Transport in Porous Media (2020) 133:139–157
https://doi.org/10.1007/s11242-020-01418-9

On the Interfacial Flow Over Porous Media Composed of Packed Spheres: Part 1-Identification of the Effective Slip Length

Jin Gang Lu[1] · **Seung Chan Cho**[2] · **Wook Ryol Hwang**[1]

Received: 8 September 2019 / Accepted: 25 April 2020 / Published online: 2 May 2020

Abstract
The effective slip length at the interface between pure fluid flow and porous media composed of packed spheres has been accurately characterized. In this study, as the first part of a two-part series, the slip length is obtained by matching the flow rate over the actual packed spheres from a direct simulation with that over an effective smooth surface using the Navier-slip boundary condition from analytic solution. Three classical packing structures, e.g., simple cubic (SC), face-centered cubic (FCC), and body-centered cubic (BCC), are employed. The accuracy of the slip length is validated by comparing the velocity field of flow over the actual porous architecture and over the effective smooth surface. We report that the slip length is best described as a function of the free slip area, rather than conventional variables such as solid volume fraction and packing structure, with the error less than 7.5%. Then, the effective smooth surface with the slip length is applied to describe two flow problems: a stick–slip–stick flow and channel flow. The slip velocity as well as its slope at the interface and the velocity profile within the pure fluid channel is accurately reproduced. In Part 2, effective slip length will be employed to characterize optimal effective viscosity and stress jump coefficient in the Stokes–Brinkman approach, which can be applied for industrial and natural flows in dual-scale porous media in predicting flow solutions inside and outside the porous media.

Keywords Navier-slip · Slip length · Packed spheres · Flows in porous media · Flow at interface

✉ Wook Ryol Hwang
wrhwang@gnu.ac.kr

[1] School of Mechanical Engineering, Research Center for Aircraft Parts Technology (ReCAPT), Gyeongsang National University, Jinju 52828, Korea

[2] Composites Research Division, Korea Institute of Materials Science, Changwon 51508, Korea

1 Introduction

Fluid flow over and/or through porous media has received attention for the last several decades. It can be widely encountered in nature or in industry, for example, migration of contaminants in soil and ground water (Bear and Verruijt 2012; Palle and Aliabadi 2016), enhanced oil recovery (Cohen and Cheng-Nian 1984), chemical reaction engineering (Davis and Stone 1993; Jafari et al. 2008), filtration (Chellam and Wiesner 1993), composites processing (Martins et al. 2009), and chromatography (Rogers and Wirth 2012; Wu et al. 2013). Studies have shown that there appears a nonzero velocity in the flow direction on a corrugated solid surface of porous media as a fluid passes. The flow enhancement caused by the slip phenomenon may provide a notable improvement, for example, in separation efficiency for chromatography (Rogers and Wirth 2012; Wu et al. 2013) and in predicting the pumping characteristics (Rajesh Kumar and Ramesh Babu 2019). In addition, accurate characterization and modeling of the interfacial slip is of great importance to understand the bubble transport through a porous channel (Gangloff et al. 2014, 2015) or particle deposition on fiber tows for advanced composites materials (Yergey et al. 2010; Hwang et al. 2011).

A number of theoretical, experimental, and numerical studies have been conducted to investigate the slip phenomenon for flows over and/or through porous media. For example, a pioneering experiment on the Poiseuille flow over a naturally permeable block performed by Beavers and Joseph (1967) reported that mass efflux was greater than that for a non-slip solid wall. A phenomenological slip boundary condition was then proposed. The velocity gradient at the interface scales with the slip velocity, i.e., $\partial u/\partial n = \left(\alpha_{\mathrm{BJ}}\Big/\sqrt{K}\right)\left(u_{\mathrm{s}} - u_{\mathrm{D}}\right)$, where α_{BJ}, K, u_{s}, and u_{D} represent the dimensionless slip coefficient, permeability, slip velocity, and Darcy velocity, respectively. The dimensionless slip coefficient α_{BJ} is considered a key parameter to assign the accurate slip boundary condition at the interface so that the flow field in the fluid channel can be accurately predicted.

However, there is no common agreement in studies on how to choose the slip coefficient as well as its dependence on both solid volume fraction and porous architecture. For example, as reported by Beavers and Joseph (1967), the dimensionless slip coefficient increases with the porosity of the foametal block. James and Davis (2001), however, found that the dimensionless slip coefficient increases as the porosity decreases in their study of the planar Couette flow and Poiseuille flow in a channel partially filled with arrays of cylinders. Liu and Prosperetti (2011) numerically investigated three-dimensional flow in a channel bounded by one (for Couette flow) and two (for Poiseuille flow) parallel porous walls modeled by packed spheres in a simple cubic (SC) arrangement. They concluded that the slip coefficient increases with the porosity, and the pressure-driven flow yields a different slip coefficient value with the shear flow. Hsu and Cheng (1991) studied the Couette flow in a channel over a semi-infinite porous medium composed of packed spheres. By matching the slip velocity with that from Beavers and Joseph (1967), the slip coefficient was found to decrease with the porosity, which is consistent with the results from James and Davis (2001) and opposite to those from Beavers and Joseph (1967) and Liu and Prosperetti (2011). Sahraoui and Kaviany (1992) examined the hydrodynamic boundary condition at the interface between a porous and plain medium by direct simulations. They concluded that the slip coefficient is a function of porous structure and is dependent on the flow direction, Reynolds number, extent of the plain medium, and non-uniformities in the arrangement of the surface particles.

In this study, we focus on flows over porous media, which are composed of packed spheres with various packing structures, e.g., simple cubic (SC), face-centered cubic (FCC), and body-centered cubic (BCC). The slip coefficient is obtained via Navier-slip length by matching the flow rate over the actual packed spheres from the direct simulation and that over an effective smooth surface using the Navier-slip boundary condition from analytic solution. The accuracy of the slip length is validated by comparing the velocity field for the flows over the actual porous media and effective smooth surface. Finally, the effective smooth surface with the slip length is employed to describe two example flow problems: a stick–slip–stick flow and channel flow bounded by porous walls. The present work might facilitate in providing an efficient framework to investigate the slip issue in porous media composed of packed spheres due to its low computational cost.

This article is organized as follows. First, we derive the expression of slip length following the original flow rate matching method by Beavers and Joseph (1967). Then, we discuss the scaling behavior of the slip length as a function of the relative free slip area. The accuracy of the slip length is validated by comparing the velocity field for an oblique flow over the actual sphere-packed porous media from the direct simulation and that over an effective smooth surface using the Navier-slip boundary condition. Finally, the effective smooth surface with the slip length is applied to solve two classical flow problems: a stick–slip–stick flow and channel flow. In both cases, the flow rates are increased owing to the presence of the corrugated architecture at the porous interface.

Before deriving the expression of slip length, we have some remarks:

(1) In this study, we focus on an idealized porous medium model composed of arrays of spheres, which are packed in strictly regular structures (e.g., SC, BCC, and FCC). The spheres are assumed to be fixed such that it could be regarded as a granular porous medium or a filter cake (Sangani and Behl 1989).
(2) The estimation of slip length depends on the choice of interface location. In this study, we choose the plane tangent to the outer edges of the spheres in the first row, as what have done in numerous studies, for example, Sangani and Behl (1989), Sahraoui and Kaviany (1992), James and Davis (2001), and Liu and Prosperetti (2011). This choice is considered most logical due to its first contact with the flow (James and Davis 2001).

2 Modeling

2.1 Expression of the Slip Length with the Flow Rate

In this section, we present the derivation of the slip length for a pressure-driven flow through and over a porous medium composed of packed spheres as shown in Fig. 1. To reduce the computational cost and clearly describe this problem, a unit flow structure is selected, as shown in Fig. 2a. The entire domain can be decomposed into two regions: the pure fluid channel ($0 < z < H$) and porous region ($z < 0$). A periodic boundary condition with and without a pressure drop (Δp) is assigned in the x- and y-directions, respectively. Neglecting the inertia, the flow in the entire domain can be described by the Stokes equation

$$\nabla p = \mu \nabla^2 \boldsymbol{u}, \tag{1}$$

where p, μ, and $\boldsymbol{u}$ denote the pressure, fluid viscosity, and velocity vector, respectively. Stokes assumption is reasonable in this work since the dependence of the slip length on the

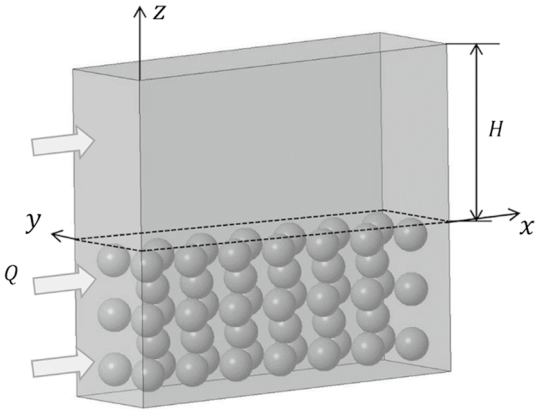

Fig. 1 A schematic description of a pressure-driven flow through and over a porous medium composed of packed spheres

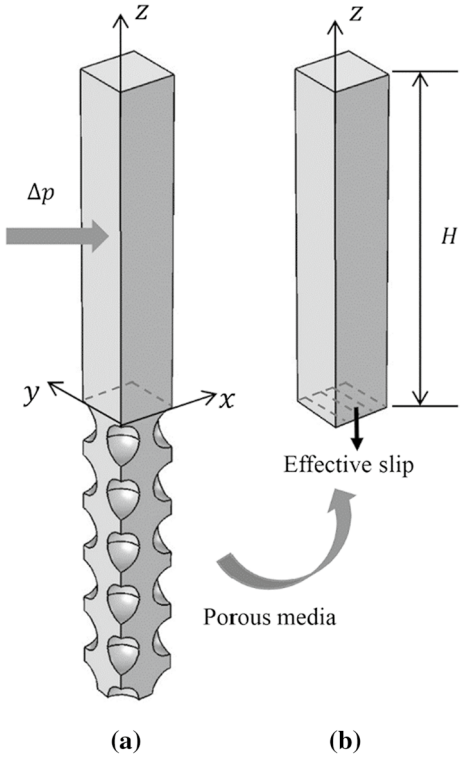

Fig. 2 The computational model for a pressure-driven flow over a three-dimensional porous media of packed spheres. **a** A model for simulation with an actual complex microstructure; **b** the corresponding flow model for the effective Navier-slip boundary condition with a fictitious smooth surface

Reynolds number is negligible as far as the flow is laminar (Jang et al. 2016). According to Beavers and Joseph (1967), when a fluid flows over porous media, there appears a nonzero slip velocity, scaling with the velocity gradient at the interface. In this regard, a fictitious smooth surface (Fig. 2b) with a slip boundary condition can be proposed to replace the actual porous media of a complicated architecture. For one-dimensional pressure-driven flow in the x-direction, the Stokes equation (Eq. 1) becomes $\mathrm{d}p/\mathrm{d}x = \mu\partial^2 u/\partial z^2$. The top

surface is considered a no-slip wall, i.e., $u = 0$ at $z = H$, and at the interface, it yields the slip boundary condition by Beavers and Joseph (1967)

$$\frac{\mathrm{d}u}{\mathrm{d}z} = \beta\left(u_\mathrm{s} - u_\mathrm{D}\right),\ z = 0, \tag{2}$$

where β is the slip coefficient; u_D is the Darcy velocity, which can be obtained from Darcy's law, i.e., $u_\mathrm{D} = -(K/\mu)\cdot \mathrm{d}p/\mathrm{d}x$. According to the governing equation and the boundary conditions given above, the solution in the fluid channel is

$$u = -\frac{1}{2\mu}\frac{\mathrm{d}p}{\mathrm{d}x}\left(\frac{H^2 + 2K\beta H}{1+\beta H} - \left(\frac{2K\beta - \beta H^2}{1+\beta H}\right)z - z^2\right). \tag{3}$$

Then, the flow rate per unit length Q_slip through the channel is obtained by integrating the velocity solution (Eq. 3) along the channel height, which is enhanced compared to that with two no-slip walls

$$Q^* = \frac{Q_\mathrm{slip}}{Q_\mathrm{no\text{-}slip}} = \left(1 + \frac{3}{1+\beta H}\left(1 + \frac{2\beta K}{H}\right)\right),\quad Q_\mathrm{no\text{-}slip} = -\frac{H^3}{12\mu}\frac{\mathrm{d}p}{\mathrm{d}x}, \tag{4}$$

where $Q_\mathrm{no\text{-}slip}$ is the flow rate with both walls subjected to no slip and Q^* is the flow rate ratio. Replacing Q_slip by actual flow rate over porous media (Fig. 2a), the slip coefficient can be obtained

$$\beta = \frac{4 - Q^*}{(Q^* - 1)H - 6K/H}. \tag{5}$$

The Beavers–Joseph slip boundary condition (Eq. 2) can be rewritten as $u_\mathrm{s} = (1/\beta)\mathrm{d}u/\mathrm{d}z + u_\mathrm{D}$. According to Saffman (1971), neglecting the Darcy velocity u_D, the remaining part of this equation, i.e., $Q_\mathrm{no\text{-}slip}$ suffices to determine the slip coefficient, which is correct to the order $O\left(\sqrt{K}\right)$, considering $1/\beta = \sqrt{K}/\alpha_\mathrm{BJ}$. On the other hand, the Navier-slip boundary condition indicates that the slip velocity at the interface is proportional to the velocity gradient, i.e., $u_\mathrm{s} = b\mathrm{d}u/\mathrm{d}z$, with b being the slip length. By comparing the simplified form of the Beavers–Joseph slip condition by Saffman (1971) with the Navier-slip boundary condition, the slip length in the Navier-slip description can be approximated as the reciprocal of the slip coefficient, i.e., $b = 1/\beta$. Then, according to Eq. (5), the expression of slip length is

$$b = \frac{(Q^* - 1)H - 6K/H}{4 - Q^*}. \tag{6}$$

2.2 Estimation of the Permeability

As indicated in Eq. (6), to evaluate the slip length correctly, the permeability K should be quantified accurately. Before investigating the slip length characterization, the permeability estimation is performed. In this study, the porous media are modeled by packed spheres and we consider three classical packing architectures: the simple cubic (SC), face-centered cubic (FCC), and body-centered cubic (BCC), as shown in Fig. 3a–c. According to Darcy's law, the permeability can be expressed as $K = -u_\mathrm{D}(\mu/(\mathrm{d}p/\mathrm{d}x))$ and we computed the permeability numerically by solving the Stokes flow problem through a three-dimensional

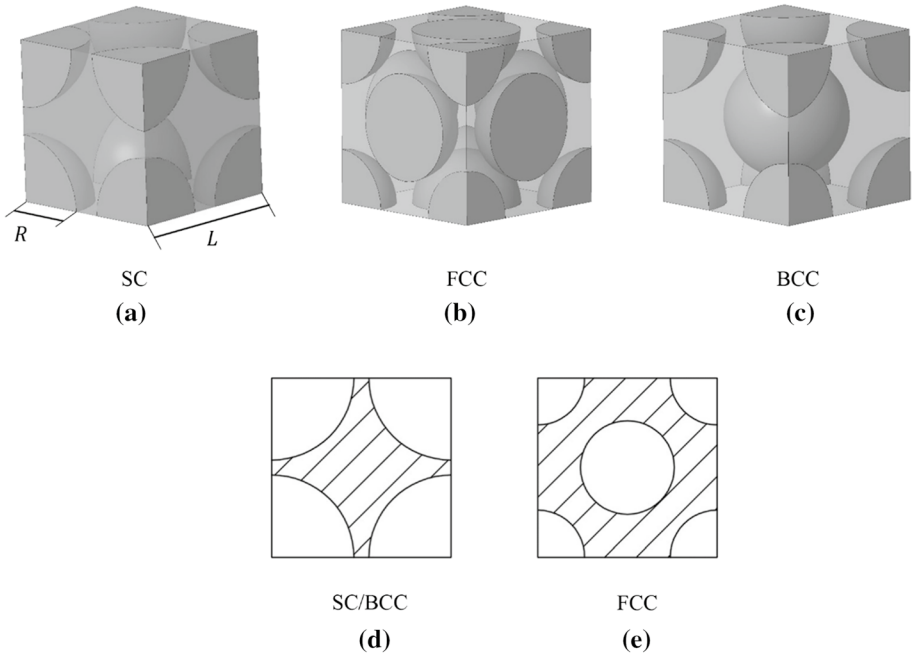

Fig. 3 Three unit porous structures of spheres with the same solid volume fraction $(\phi_s = 0.3)$. **a** The simple cubic (SC), with the dimensionless free surface area $A^* = 0.458$; **b** the face-centered cubic (FCC), with $A^* = 0.570$; **c** the body-centered cubic (BCC), with $A^* = 0.659$; **d** free slip area for the SC and BCC packing structures; **e** free slip area for the FCC packing structure

unit cell with a periodic boundary condition subjected to a given pressure drop in the flow direction. A similar method for computing the permeability in a two-dimensional bi-periodic unit cell is shown in previous studies, such as Lu et al. (2017) and Wang and Hwang (2008). COMSOL 5.2 with a quadratic velocity and linear pressure interpolations is employed to implement the simulations in this work. When estimating the permeability, the entire unit cell is discretized by three-dimensional free tetrahedral meshes. Although not presented, we tested the accuracy of the solution with the mesh refinement and evaluated the convergence to ensure the accuracy in estimating the permeability and later the slip lengths. Figure 4 shows the normalized permeabilities (normalized by the square of the sphere radius R^2) of three different porous architectures (SC, FCC, and BCC) for a wide range of solid volume fractions along with the prediction by Happel (1958) for comparison. According to Happel (1958), the empirical equation to estimate the normalized permeability for porous media composed of packed spheres can be expressed as

$$\frac{K}{R^2} = \frac{3 - 3\phi_s^{1/3} + 3\phi_s^{5/3} - 2\phi_s^2}{9\phi_s + 6\phi_s^{8/3}}, \tag{7}$$

where ϕ_s is the solid volume fraction. A minor discrepancy is shown between the results by Happel (1958) and those in this study for the densely and lightly packed structures. However, there was approximately a 24.5% discrepancy for the FCC structure when the porous media are moderately packed, which implies the empirical equation from Happel

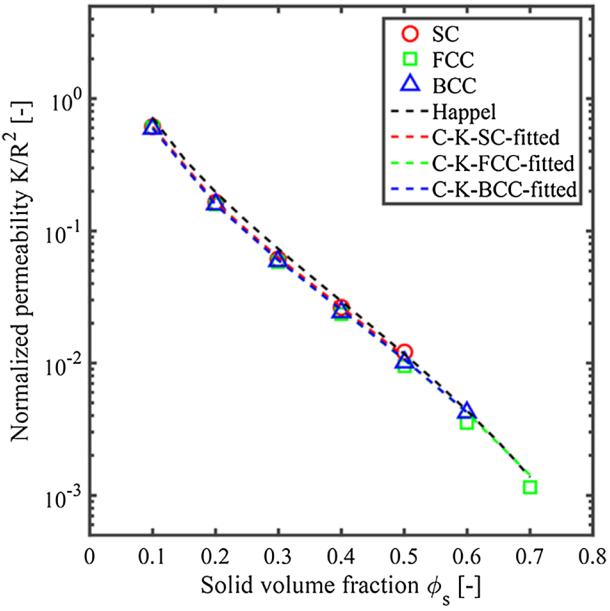

Fig. 4 The normalized permeability as a function of the solid volume fraction for three different porous architectures (SC, FCC, and BCC) along with the empirical prediction from Happel (1958) and fitted Carman–Kozeny constants

(1958) may not be appropriate. In addition, the Carman–Kozeny model (1997) is widely used to characterize the correlation between the permeability and solid volume fraction. This model can be expressed as

$$\frac{K}{R^2} = A\frac{\left(1-\phi_s\right)^3}{\phi_s^2}, \tag{8}$$

where A is the Carman–Kozeny constant. It can be decomposed into two factors such that $A = a\phi_s^b$, with the contribution from the porous architecture (a) and that from the solid volume fraction $\left(\phi_s^b\right)$. The parameters a and b, obtained by fitting the computational results using the least squares method, are 0.0343 and 0.610 for the SC structure, 0.0320 and 0.590 for the FCC structure, and 0.0323 and 0.598 for the BCC structure. In Fig. 4, fitted curves for each packing structure from the Carman–Kozeny prediction are also shown. The slip length in a closed form can then be accurately characterized, with the permeabilities estimated above.

2.3 Slip Length and Its Universal Behavior

After obtaining the permeability, a direct simulation for the flow over the actual packed spheres (Fig. 2a) is performed to determine the slip length. The direct flow simulation has been performed by COMSOL 5.2 with quadratic velocity and linear pressure interpolations. As reported by James and Davis (2001), the slip coefficient/length depends nearly on the outmost microstructure of the interface. Thus, five layers of the porous structure are considered adequate in this study. A periodic boundary condition with and without a pressure drop is assigned in the x-and y-directions, respectively. The flow rate Q_{slip} through the channel from the direct simulation is substituted into Eq. (4) to obtain the flow rate ratio Q^*, which

is employed to compute the value of the slip length according to Eq. (6). Figure 5 shows the dimensionless slip length $b^* = b/R$, with R being the radius of a sphere, as a function of the solid volume fraction with two dimensionless channel heights ($H/R = 16$ and 32) for three different porous architectures. For each packing structure, a minor discrepancy of the slip length is shown with different channel heights, which is consistent with the conclusion in the authors' previous work (Lu et al. 2017) for the two-dimensional fibrous porous media such that the dependence of slip length on flow channel height is nearly negligible for sufficiently large channel height ($H/R >> O(1)$). The dimensionless slip lengths are found to decrease as the solid volume fractions increase. For the same solid volume fractions, the BCC structure yields the largest value of the slip length, while the SC structure shows the smallest one. To explain this, a measure of the relative free slip area (A^*) is introduced, and as will be shown, it can be regarded as a characteristic parameter representing the magnitude of the interfacial slip. As shown in Fig. 3d, e, the relative free slip area is defined as

$$A^* = 1 - \frac{N\pi R^2}{L^2}, \tag{9}$$

where '1' denotes the area ratio of the top surface for a unit porous structure, i.e., $1 = L^2/L^2$; N is the number of spheres within the top surface. For the SC and BCC structures, the value of N is 1, and for FCC structure, N is 2. In fact, $Q_{\text{no-slip}}$ is the ratio between the free slip area (area with a pattern in Fig. 3d, e) and unit surface area $\left(L^2\right)$. For packed spheres, the correlation between $Q_{\text{no-slip}}$ and the solid volume fraction ϕ_s can be expressed as $Q_{\text{no-slip}}$, with $n = 1,\ 2,$ and 4 for the SC, BCC, and FCC, respectively. Figure 6 shows the dimensionless slip lengths as a function of the relative free slip area for different channel heights ($H/R = 16$ and 32) and various porous architectures. For the dimensionless channel height of 32 ($H/R = 32$), the fitted curve can be provided as: $b^* = c(A^*)^e + \delta$. The reference slip δ represents the slip length when the spheres are completely packed (two

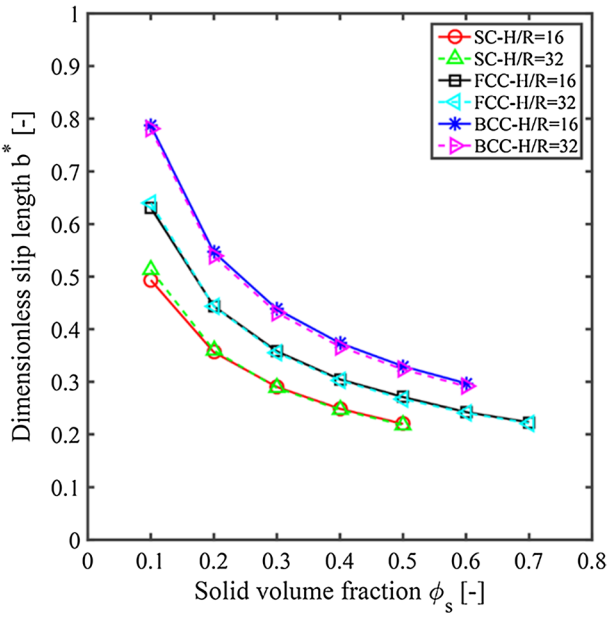

Fig. 5 The dimensionless slip length as a function of the solid volume fraction for three different porous architectures with two different dimensionless channel heights ($H/R = 16$ and 32)

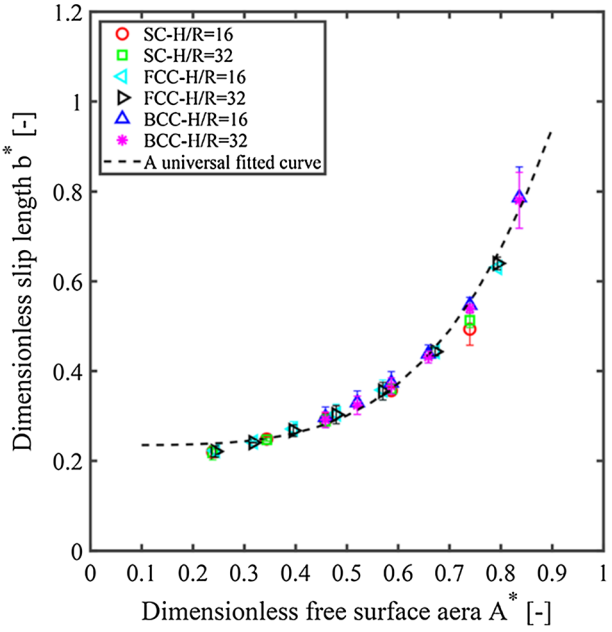

Fig. 6 The dimensionless slip length as a function of the relative free slip area for different porous architectures along with a universal fitted 'master' curve. The absolute error bars are also presented

closest spheres in contact with each other). The exponent e indicates how fast the slip length increases with the relative free slip area and c is a constant. The fitted results are

$$b^* = \begin{cases} 0.725A^{*2.906} + 0.210, & \text{SC} \\ 0.922A^{*3.473} + 0.223, & \text{FCC} \\ 1.228A^{*4.959} + 0.273, & \text{BCC} \end{cases}. \tag{10}$$

All the data of the dimensionless slip lengths along with the relative free slip areas for the three different packing structures are listed in Table 1. One can observe that, for the same solid volume fraction, the BCC structure yields the largest relative free slip

Table 1 The dimensionless slip length (b^*) and dimensionless slip coefficient (α_{BJ}) along with the relative free slip area (A^*) as a function of the solid volume fraction for three different porous architectures (SC, FCC, and BCC)

ϕ_s	SC				FCC				BCC			
	K/R^2	A^*	b^*	α_{BJ}	K/R^2	A^*	b^*	α_{BJ}	K/R^2	A^*	b^*	α_{BJ}
0.1	0.613	0.740	0.513	1.526	0.598	0.793	0.640	1.209	0.595	0.836	0.780	0.988
0.2	0.165	0.587	0.360	1.129	0.160	0.672	0.443	0.901	0.159	0.740	0.539	0.740
0.3	0.062	0.458	0.288	0.862	0.059	0.570	0.355	0.683	0.059	0.659	0.431	0.563
0.4	0.026	0.344	0.247	0.657	0.024	0.479	0.303	0.507	0.024	0.587	0.367	0.425
0.5	0.012	0.238	0.218	0.505	0.009	0.396	0.267	0.364	0.010	0.520	0.324	0.312
0.6	–	–	–	–	0.004	0.317	0.241	0.246	0.004	0.458	0.291	0.223
0.7	–	–	–	–	0.001	0.243	0.221	0.154	–	–	–	–

area, which might be responsible for the largest slip length with the largest reference slip δ and fastest exponent e, see Eq. (10).

It is interesting to observe that all the data could be fitted into a single master curve in spite of the different structures. Figure 6 shows a universal scaling behavior for the slip length, and a master curve can be expressed as

$$b^* = A^{*4} + 0.23. \tag{11}$$

At the same time, the absolute error bars have been also presented in Fig. 6. From now on, one can readily obtain the value of the slip length for porous media of packed spheres with Eq. (11), once the relative free slip area or the solid volume fraction is given. In addition, with the correlation between the dimensionless slip coefficient α_{BJ} and dimensionless slip length b^*, i.e., $\alpha_{\mathrm{BJ}} = b^* \sqrt{K} \Big/ R$, the value of α_{BJ} can also be obtained according to Eqs. (8) and (11). Figure 7 shows the dimensionless slip coefficients as a function of the solid volume fraction for different porous architectures along with the result for the SC structure by Liu and Prosperetti (2011) for comparison. For various porous architectures, the dimensionless slip coefficients are found to decrease with solid volume fraction, which agrees with Beavers and Joseph (1967) and Liu and Prosperetti (2011). The SC structure has the largest value of the slip coefficient for the same solid volume fraction, whereas the FCC structure yields the smallest one. There is a good agreement between the estimation of the slip coefficients for the SC structure by Liu and Prosperetti (2011) and that obtained in this study. A maximum discrepancy of approximately 6% appears, when the solid volume fraction is around 0.155. The dimensionless slip coefficients for the three packing structures are also listed in Table 1.

To understand the effect of a small perturbation of the sphere position on the slip length, a sphere located at the center of a unit cubic for the BCC structure has been moved with a distance Δs in both the horizontal (leftward shift) and vertical (upward or

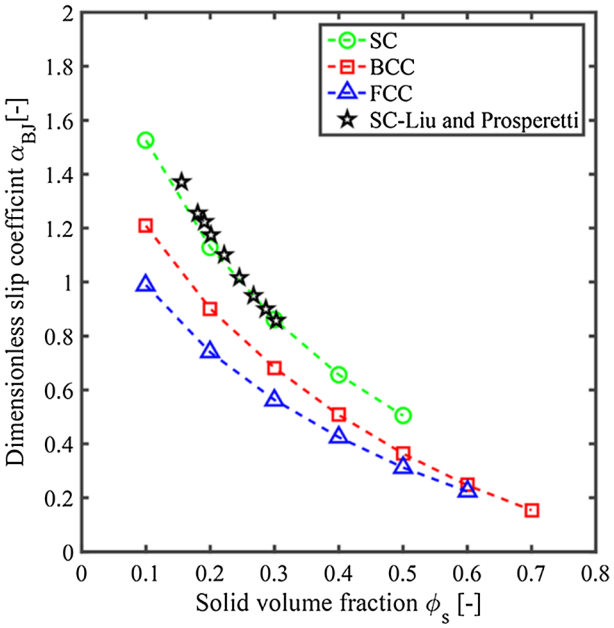

Fig. 7 The dimensionless slip coefficients as a function of the solid volume fraction for different porous architectures. (The dimensionless slip coefficients for the simple cubic (SC) structure by Liu and Prosperetti (2011) are also presented for comparison)

downward shift) directions, see Fig. 8. The solid volume fraction ϕ_s is set 0.2, and $\Delta s/L$ is 0.125. It has been found that the values of the dimensionless slip length are 0.538 for the leftward case, 0.535 for the upward case, and 0.540 for the downward case, respectively. In comparison with the original value of the slip length ($b^* = 0.539$), in Table 1, the slip length for the horizontal and downward shifts remains unchanged. Only the case with upward move yields a slightly reduction in the slip length, due to decrease of free fluid volume beneath the interface. It is noted that even for the upward shift, the relative error of the dimensionless slip length is found around 0.74%, which could be considered neglected. Therefore, the fitted model proposed in the present work might be still applicable with the presence of a small perturbation of the sphere position.

Before moving to the next section, we would like to mention that the idea correlating the slip length/coefficient with the geometric parameter at the interface can be extended to more general cases, e.g., the complete randomly packed spheres. The average dimensionless free surface area can be obtained by seeking the ratios of the free surface area to the total surface area among a large amount of cross sections beneath the interface. It is expected that, for a given solid volume fraction, the final value of the average dimensionless free surface area will show statistically complicated behaviors from numerous samples of randomly packed spheres. Therefore, the slip length might be expressed in terms of the average dimensionless free surface area. Besides, in the case of randomly packed spheres, some details still need further considerations, for example, the choice of the position of the interface as well as the optimal statistical methods to be applied. In addition, the measurement of the local velocity fields around the interface for the randomly packed spheres and the work by Saleh et al. (1993), for example, may serve as a reliable reference to validate the accuracy of the theoretical and numerical results.

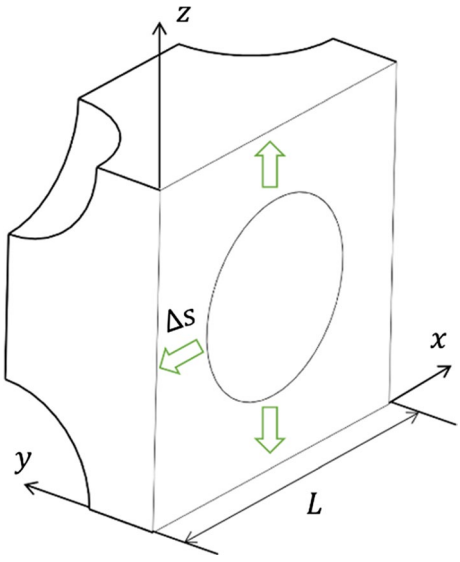

Fig. 8 The effect of a minor randomness of the sphere position on the slip length for the BCC structure. The solid volume fraction ϕ_s is 0.2, and the movement distance of the central sphere in both the horizontal (leftward shift) and vertical (upward or downward shift) directions $\Delta s/L = 0.125$

3 Verification of the Slip Length and Example Flow Problems

3.1 Verification of the Slip Length

In order to evaluate the accuracy of the slip length, an oblique flow problem over the porous media with SC structure is solved, in which the local coordinate (xy) is not conforming with the global coordinate system (XY) as shown in Fig. 9a. A pressure drop is assigned in the x-direction. The local tensor form of the Navier-slip condition at the interface can be expressed as

$$\boldsymbol{u}_{\text{slip}} = \boldsymbol{b} \cdot (\boldsymbol{n} \cdot \nabla \boldsymbol{u}), \tag{12}$$

where $\boldsymbol{b}$ is the slip length tensor. As the porous structure is isotropic and thereby the slip length tensor is $\boldsymbol{b} = \text{diag}(b, b)$. Then, each component of the slip velocity vector at the interface can be expressed in terms of the velocity gradient with the slip length

$$u = b\frac{\partial u}{\partial z}, \quad v = b\frac{\partial v}{\partial z}. \tag{13}$$

For this flow problem shown in Fig. 9, the porous structure is chosen as SC with the solid volume fraction $\phi_s = 0.3$ and the alignment angle $\theta = 30°$. The width of the periodic domain is 1 (mm), and the radius of the sphere R is 415 (μm). The height of the flow channel above the spheres is set as $H = 32R$. According to Jang et al. (2016), flow characteristics within a groove, which is analogous to the flow on the porous surface, do

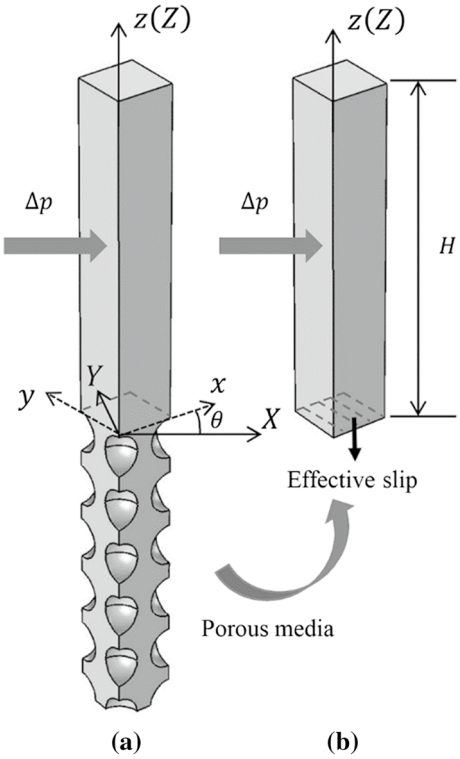

Fig. 9 The computational model for an oblique flow over a three-dimensional porous medium of packed spheres. **a** A model for the direct simulation with the actual complex microstructure; **b** the corresponding flow model for the effective Navier-slip boundary condition with a fictitious smooth surface. Local coordinate system (xy) is not consistent with the global coordinate system (XY)

not change with respect to the Reynolds number in the Laminar regime. Thus, neglecting the inertia effect owing to the small scale of the flow problem, a full three-dimensional direct simulation is implemented to solve the Stokes flow problem over the porous media composed of packed spheres. With the geometry parameters given above, the dimensionless slip length is obtained from Eq. (11) or Table 1, which is 0.288 and thereby the slip length $b = b^* \cdot R = 1.2 \times 10^{-4}$ (m). The corresponding simulation with an effective surface and a slip boundary condition expressed by Eq. (13) is then conducted. Velocity profiles within fluid channel in each component from the direct simulation (Fig. 9a) and from the corresponding simulation with effective surface (Fig. 9b) are shown in Fig. 10. One can observe that the velocity profiles in each component from the direct simulation agree well with those from the simplified simulation with an effective smooth surface. The maximum relative errors are found to be 1.84% and 1.83% in the x- and y-component, respectively. In addition, at the interface ($H/R = 0$), the presence of slip velocity around 3.1% and 1.79% of the maximum velocity in the x- and y-components can be identified. The slip velocity in the x-component is approximately 1.73 times of that in the y-component due to the prescribed alignment angle ($\theta = 30°$). Having validated the accuracy of the slip length, in next section, the Navier-slip condition with the slip length will be employed to solve two complicated flow problems.

3.2 Stick–Slip–Stick Flow and Channel Flow Problems

In this section, two practical example flow problems are solved: stick–slip–stick flow and pressure-driven channel flow with a rectangular cross section. The first flow problem is the stick–slip–stick flow problem as shown in Fig. 11. A direct simulation (Fig. 11a) is first conducted for a pressure-driven flow over two aligned no-slip solid walls, which are

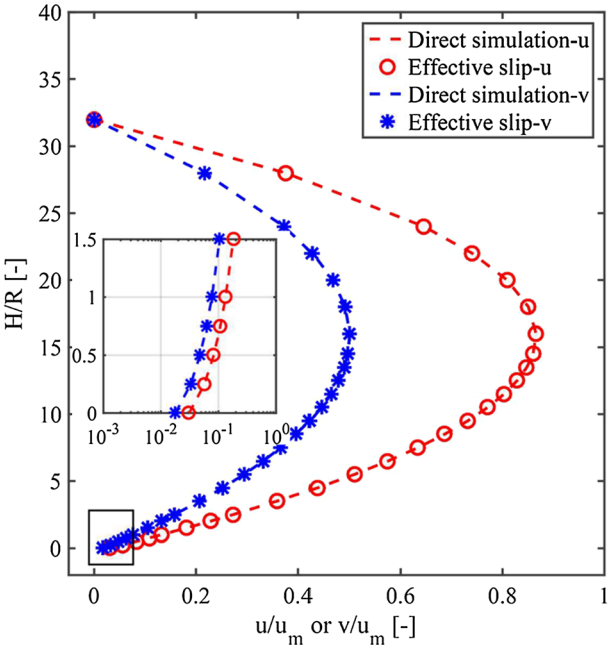

Fig. 10 The velocity profiles in each component within the fluid channel from both the direct simulation and from the simulation with effective slip surface

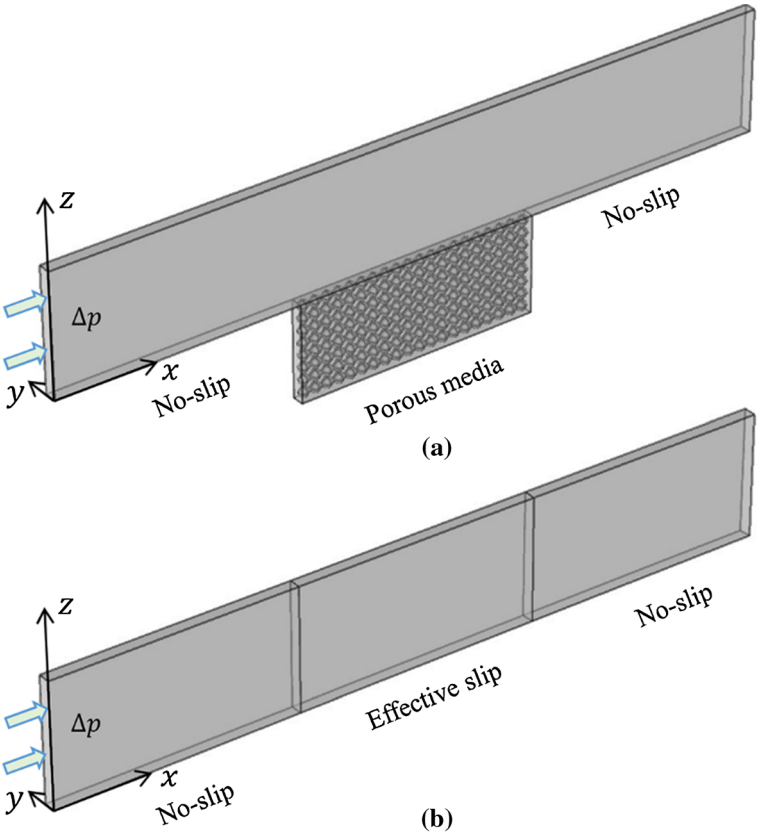

Fig. 11 A schematic description of the stick–slip–stick flow problem: **a** the computational domain for flow over the actual porous media composed of packed spheres; **b** the computational domain for flow over an effective smooth surface with the Navier-slip boundary condition

connected by a porous surface composed of packed spheres. A periodic boundary condition with and without a pressure drop is assigned in the x- and y-directions, respectively. All the remaining boundaries are subjected to no-slip walls. The porous medium is composed of eight layers of spheres, which are packed in the SC structure. The sphere size and solid volume fraction are chosen to be the same as those in the flat channel flow problem in Sect. 3.1. The length (x-direction) and the thickness (y-direction) of the entire computational domain are 6 (mm) and 0.1 (mm), respectively. For an effective simulation (Fig. 11b), the actual porous architecture is replaced by a smooth surface subjected to the Navier-slip boundary condition: $u = b\partial u/\partial z$, with the slip length b of 1.2×10^{-4} (m). COMSOL 5.2 with the quadratic velocity and linear pressure interpolations is employed to implement the simulations. Although not presented here, we tested the accuracy of the solution with the mesh refinement and evaluated the convergence. Increase of the flow rate through the channel is found in both the direct and effective simulations compared to that subjected to a complete no-slip solid bottom wall. The flow rate ratios $\left(Q^* = Q_{\text{slip}}/Q_{\text{no-slip}}\right)$ are found to be 1.0117 and 1.0115 for the direct and the effective simulations, respectively.

Figure 12 shows the velocity profiles along a centerline located in the bottom surface (Fig. 11) from both the direct simulation and the effective simulation with the Navier-slip condition. In the upstream region, the velocity from the direct simulation is zero owing to the no-slip property of the solid wall. Then, the velocity increases sharply and there is a fluctuation between 3.9 and 4.9% of the maximum velocity caused by the periodic structure of porous media at the interface. The velocity decreases to zero along the downstream region. The velocity from the simulation with an effective smooth surface is found to be close to the average fluctuation velocity from the direct simulation, and the mean velocity, which is computed from the data of the direct simulation over the porous surface, is approximately 98.6% of that in the effective simulation. The result shows that the slip boundary condition with slip length reproduces flow characteristics accurately.

The second example flow problem is a rectangular channel flow bounded by 4-layers porous walls attached to the left, right, and top surfaces and one no-slip solid wall on the bottom, as shown in Fig. 13. The local porous architecture is chosen to be the same as that applied in the stick–slip–stick flow problem. The width of the channel (excluding the porous layers) is 1.917 (mm), and the height is 1.958 (mm). For the direct simulation (Fig. 13a), a periodic boundary condition with and without a pressure drop has been assigned in the y- and x-directions, respectively. A symmetry boundary condition is defined on the top porous surface, whereas the bottom surface yields a no-slip wall. For the simulation with effective surfaces (Fig. 13b), the porous structure is replaced by three smooth surfaces with the Navier-slip boundary conditions, in which the slip length is 1.2×10^{-4} (m). Before quantitatively validating the accuracy of the Navier-slip boundary condition with the slip length, the effect of the number of porous layers on the flow rate through the channel and on the average slip velocity at the interface are investigated first. As shown in Fig. 14, the flow rate through the channel is enhanced compared to that if all the channel walls were impermeable and the flow rate ratio is maintained by a value of approximately 1.038 ($Q^* = 1.038$), as the number of the porous layers increases from one to four.

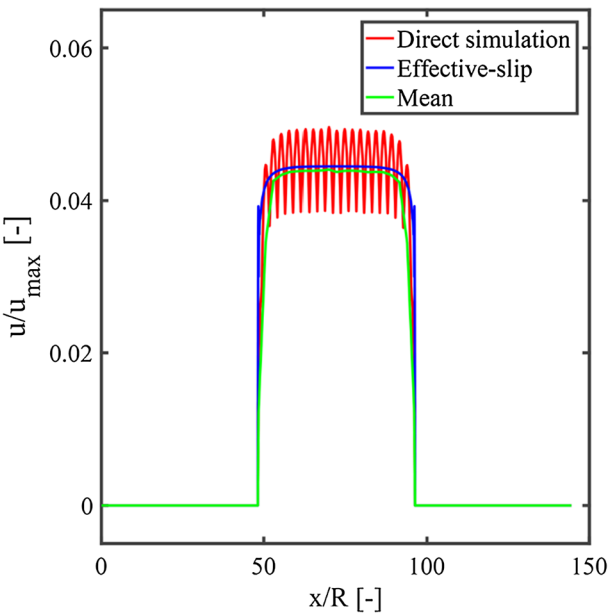

Fig. 12 The velocity profile along a centerline located on the bottom surface for the 'stick–slip–stick' flow problem (Fig. 11) from both the direct simulation and the simulation of effective slip surface. The mean velocity from the direct simulation is also presented for comparison

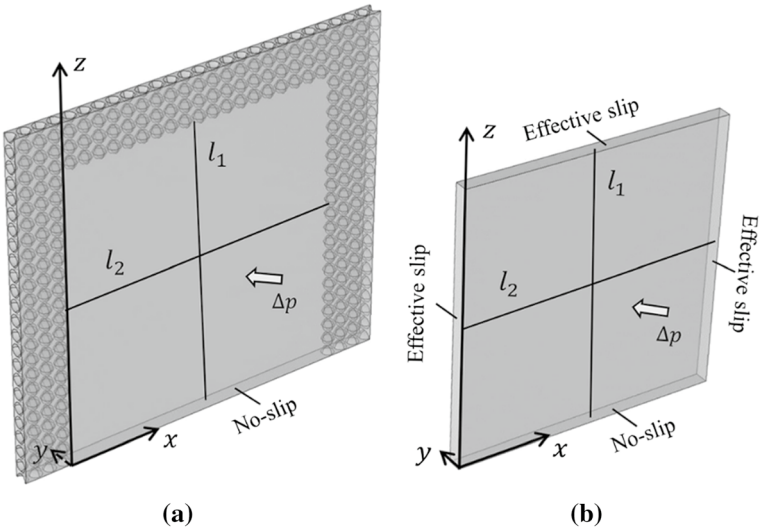

Fig. 13 A schematic description of the rectangular channel flow problem: **a** a direct simulation for the channel flow bounded by porous walls adjacent to the left, right, and top surfaces; **b** the corresponding effective simulation for the channel flow bounded by three fictitious smooth surfaces (on the left, right, and top surfaces) with the Navier-slip boundary condition

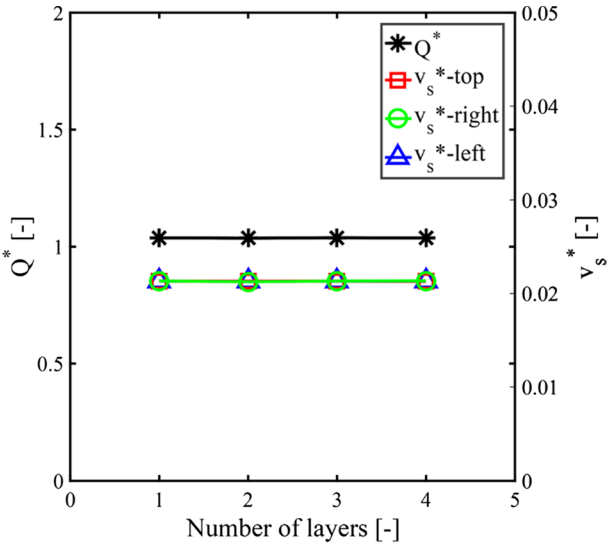

Fig. 14 Flow rates and the average slip velocity at each surface as a function of the number of porous layer

The averaged dimensionless slip velocity defined as $v_s^* = v_s / v_{\max}$ on all the three permeable surfaces yields the same value and is independent of the number of the layers, which implies that the interfacial slip is nearly affected by the outmost layer of the spheres.

Figure 15 shows the slip velocity profiles on the top [$z = 1.958$ (mm)] and left [$x = 0$ (mm)] surfaces from the direct simulation as well as from the simulation with effective surfaces (Fig. 13). As expected, the oscillation occurs from the direct simulation owing

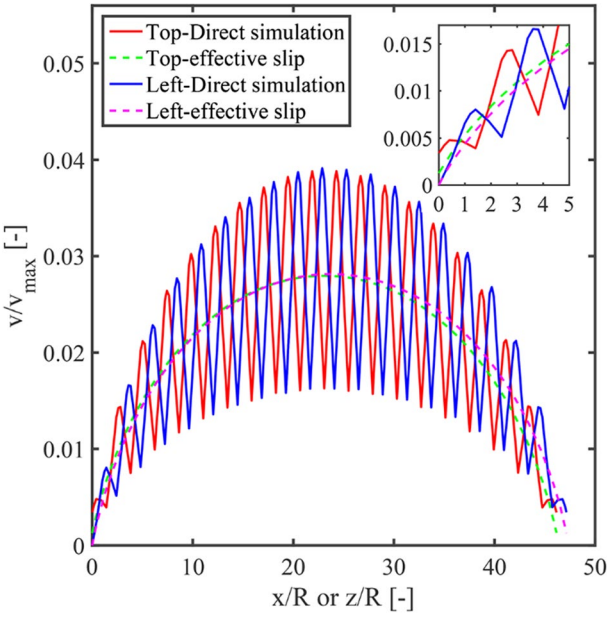

Fig. 15 The average slip velocity profiles on the top and right surfaces (Fig. 13) from both the direct simulation over actual porous media of packed spheres and the simulation with fictitious smooth surface

to the presence of periodic architectures of the packed spheres at the interface. Velocities from the simulation with effective surfaces are again located at the corresponding average positions of the oscillations, verifying that the applied effective smooth surfaces with the slip lengths are accurate. The maximum slip velocities on both surfaces (top and left) appear in the central regions. For the left surface, the velocity starts at zero due to the no-slip boundary condition of the solid bottom surface of the channel, whereas the top surface shows approximately 0.34% and 0.13% of the maximum velocity even at the top corners from both simulations, respectively. Finally, the velocity field across the channel is evaluated. The velocity distributions along the vertical line (marked as) and the horizontal line (marked as l_2), see Fig. 13, are presented to validate the accuracy of the Navier-slip boundary condition with the slip length. As shown in Fig. 16, velocities from the effective simulation for the two lines agree well with those from the direct simulation. A small discrepancy appears only within one radius distance from the interface ($x/R < 1,\ z/R < 1$). The predictions of the slip velocity at the interface are 2.1% and 2.8% of the maximum velocity from the direct and effective simulations, respectively. The effective surfaces with the Navier-slip length are found to accurately reproduce both the local slip velocity distributions on the porous surfaces and the macroscopic velocity field across the channel.

4 Conclusions

In this study, we solved the interfacial slip flow problem over porous media composed of spheres with various packing structures, such as SC, FCC, and BCC. The slip length was obtained by matching the flow rate for the flow over the actual packed spheres from the direct simulation and that over an effective smooth surface using the Navier-slip boundary condition. The accuracy of the slip length was validated by comparing the flow field of an oblique channel flow over the actual porous media and the effective smooth surface. The

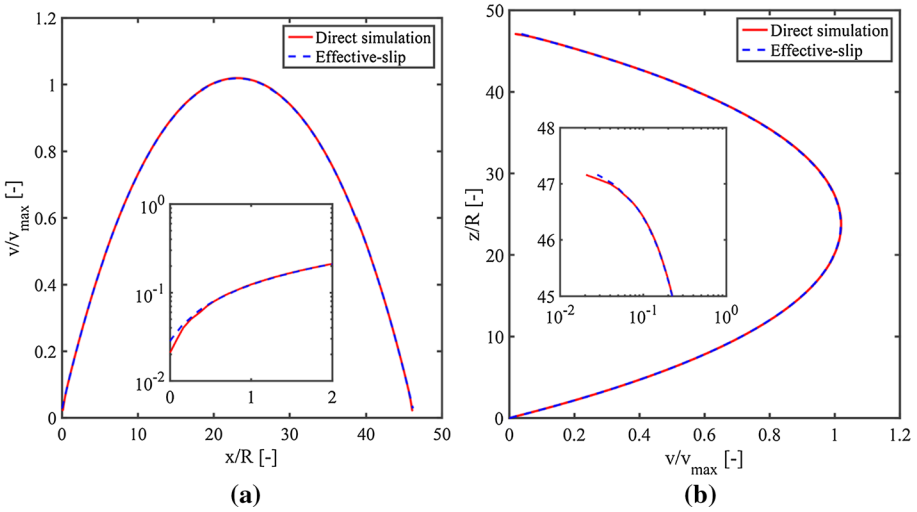

Fig. 16 The macroscopic velocity profiles across the channel along two lines within the fluid region (marked as l_1 and l_2 in Fig. 13) from both the direct simulation over the actual sphere-packed porous media and the simulation with the fictitious smooth surface

slip length is best described as a function of free slip area, rather than conventional variables such as solid volume fraction and packing structure, with the error less than 7.5%. Finally, the effective smooth surface with the slip length was applied to describe two example flow problems: a stick–slip–stick flow and channel flow. The flow rate increased in both cases owing to the presence of the corrugated surface at the interface. The average slip velocity at the interface as well as the velocity profile within the entire domain was accurately reproduced using the effective Navier-slip boundary condition.

In Part 2, effective slip length of the Navier-slip condition will be employed to characterize optimal values of the effective viscosity and stress jump coefficient in the Stokes–Brinkman approach (one with effective Brinkman viscosity and the other with the stress jump coefficient in the Ochoa-Tapia/Whitaker modeling), which can be applied for industrial and natural flows in dual-scale porous media in predicting flow solutions inside and outside the porous media.

Acknowledgements The authors acknowledge financial supports from the National Research Foundation of Korea (NRF-2019R1A2C1003974) and the Fundamental Research Program (PNK6160) of the Korea Institute of Materials Science (KIMS).

References

Bear, J., Verruijt, A.: Modeling Groundwater Flow and Pollution. Springer, Berlin (2012)
Beavers, G.S., Joseph, D.D.: Boundary conditions at a naturally permeable wall. J. Fluid Mech. **30**(1), 197–207 (1967)
Carman, P.C.: Fluid flow through granular beds. Chem. Eng. Res. Des. **75**, S3–S48 (1997)
Chellam, S., Wiesner, M.R.: Slip flow through porous media with permeable boundaries: implications for the dimensional scaling of packed beds. Water Environ. Res. **65**(6), 744–749 (1993)
Cohen, Y., Cheng-Nian, C.: The flow of microemulsions through packed beds and capillary tubes. Chem. Eng. Commun. **28**(1–3), 73–84 (1984)

Davis, R.H., Stone, H.A.: Flow through beds of porous particles. Chem. Eng. Sci. **48**(23), 3993–4005 (1993)
Gangloff Jr., J.J., Hwang, W.R., Advani, S.G.: Characterization of bubble mobility in channel flow with fibrous porous media walls. Int. J. Multiph. Flow **60**, 76–86 (2014)
Gangloff Jr., J.J., Hwang, W.R., Advani, S.G.: The investigation of bubble mobility in channel flow with wavy porous media walls. Int. J. Multiph. Flow **70**, 1–14 (2015)
Happel, J.: Viscous flow in multiparticle systems: slow motion of fluids relative to beds of spherical particles. AIChE J. **4**(2), 197–201 (1958)
Hsu, C.T., Cheng, P.: A singular perturbation solution for Couette flow over a semi-infinite porous bed. J. Fluids Eng. **113**(1), 137–142 (1991)
Hwang, W.R., Advani, S.G., Walsh, S.: Direct simulations of particle deposition and filtration in dual-scale porous media. Compos. A Appl. Sci. Manuf. **42**(10), 1344–1352 (2011)
Jafari, A., Zamankhan, P., Mousavi, S.M., Pietarinen, K.: Modeling and CFD simulation of flow behavior and dispersivity through randomly packed bed reactors. Chem. Eng. J. **144**(3), 476–482 (2008)
James, D.F., Davis, A.M.: Flow at the interface of a model fibrous porous medium. J. Fluid Mech. **426**, 47–72 (2001)
Jang, H.K., Kim, Y.J., Woo, N.S., Hwang, W.R.: Tensorial Navier-slip boundary conditions for patterned surfaces for fluid mixing: numerical simulations and experiments. AIChE J. **62**(12), 4574–4585 (2016)
Liu, Q., Prosperetti, A.: Pressure-driven flow in a channel with porous walls. J. Fluid Mech. **679**, 77–100 (2011)
Lu, J., Jang, H.K., Lee, S.B., Hwang, W.R.: Characterization on the anisotropic slip for flows over unidirectional fibrous porous media for advanced composites manufacturing. Composites A Appl Sci Manuf **100**, 9–19 (2017)
Martins, A.A., Laranjeira, P.E., Braga, C.H., Mata, T.M.: Modeling of transport phenomena in porous media using network models. In: Tian, K.S., Shu, H.-J. (eds.) Progress in Porous Media Research. Nova Science Publishers, New York (2009)
Palle, S., Aliabadi, S.: Computational study of no-slip and rarefied slip flows in infinite structured porous media. Comput. Fluids **136**, 485–496 (2016)
Rajesh Kumar, P., Ramesh Babu, V.: Effect of complete slip on peristaltic transport of Jeffrey fluid flow in a tappered channel with suction and junction. Int J Mech Eng Technol **10**(2), 551–560 (2019)
Rogers, B.J., Wirth, M.J.: Slip flow through colloidal crystals of varying particle diameter. ACS Nano **7**(1), 725–731 (2012)
Saffman, P.G.: On the boundary condition at the surface of a porous medium. Stud Appl Math **50**(2), 93–101 (1971)
Sahraoui, M., Kaviany, M.: Slip and no-slip velocity boundary conditions at interface of porous, plain media. Int. J. Heat Mass Transf. **35**(4), 927–943 (1992)
Saleh, S., Thovert, J.F., Adler, P.M.: Flow along porous media by particle image velocimetry. AIChE J. **39**(11), 1765–1776 (1993)
Sangani, A.S., Behl, S.: The planar singular solutions of Stokes and Laplace equations and their application to transport processes near porous surfaces. Phys Fluids A Fluid Dyn **1**(1), 21–37 (1989)
Wang, J.F., Hwang, W.R.: Permeability prediction of fibrous porous media in a bi-periodic domain. J. Compos. Mater. **42**(9), 909–929 (2008)
Wu, Z., Rogers, B.J., Wei, B., Wirth, M.J.: Insights from theory and experiments on slip flow in chromatography. J. Sep. Sci. **36**(12), 1871–1876 (2013)
Yergey, B.A., Beninati, M., Marshall, J.S.: Sensitivity of incipient particle motion to fluid flow penetration depth within a packed bed. Sedimentology **57**(2), 418–428 (2010)